Available online at www.sciencedirect.com
ScienceDirect
International Journal of Rock Mechanics & Mining Sciences 44 (2007) 942–947
International Journal of Rock Mechanics and Mining Sciences
www.elsevier.com/locate/ijrmms

Technical note

Digital image analysis of fluid inclusions

Jinming Xu[a,*], Xiaobo Zhao[a], Bin Liu[b]

[a]Department of Civil Engineering, Shanghai University, Shanghai 200072, PR China
[b]Department of Geotechnical Engineering, Tongji University, Shanghai 200092, PR China

Received 23 July 2006; received in revised form 22 December 2006; accepted 12 January 2007
Available online 6 March 2007

Abstract

Fluid inclusions commonly exist in the cracks of rock masses. From a microscopic point of view, the fluid inclusion plane (FIP) is the crack plane while the fluid inclusion line (FIL) is the intersecting line between a specific plane (horizontal or different) and the FIP. These microscopic compositions or structures not only provide valuable information on the deformations and/or fractures of rocks but also reflect the trend, length and width of cracks. This paper presents the digital image analysis of fluid inclusions in rocks and discusses the characteristics of FILs. For the image analysis, the original digital images photographed by the microscope equipped with a digital camera on a heating–freezing platform were first converted into grayscale images and then broken into blocks using quadtree decomposition and region segmentation. For each block, the inflection point, derivative, frequency and color-based methods were used to detect the edges of fluid inclusions. To better define the boundaries of fluid inclusions, the dilation, erosion, seed filling, boundary connection and smoothing techniques were used to, respectively, extend edges, connect discontinuous points, fill pores in the outlines, eliminate irrelative parts in neighboring positions, smoothen projecting parts around the outlines and aggregate smaller inclusions into larger ones. After the boundaries of fluid inclusions were defined, the blocks were re-assembled and the edge points and lines of fluid inclusions were then defined in a global coordinate system. Based on the geometrical properties of the fluid inclusions, such as the centroid positions, areas and long-axis directions, FILs and their configuration parameters (such as length, mean width and abundance) were obtained with the least-squares method. All of these procedures were coded into a program and could be automatically run. The digital image analyses of fluid inclusions may provide valuable information about the relationships between the FIL networks and the crack properties.

Keywords: Fluid inclusion; Image analysis; Geometrical and configuration parameters; Fluid inclusion lines

1. Introduction

Fluid inclusions commonly exist in the cracks of rock masses. From a microscopic point of view, fluid inclusion planes (FIP) are cracks which trap fluid in the form of fluid inclusions [1–3], and which will indicate superposed brittle deformations over time [4]. A fluid inclusion line (FIL) is the intersecting line between a specific plane (horizontal or otherwise) and the FIP. These microscopic compositions or structures not only provide valuable information on deformations and/or fractures of rocks, but also reflect the geometrical or configuration properties (such as trend, length and width) of cracks. Lespinasse and Cathelineau [5] recognized that FIPs are the only way to understand extensional stresses in rocks and determine the fossil fluid pathways. In recent years, much progress has been made in studying rocks using digital image analysis. Zhao and Xu [6] obtained some digital properties of geo-material images. Zhu et al. [7] developed a digital-image-based finite element technique to characterize microscopic heterogeneity. Chen et al. [8] revealed a two-dimensional digital image-based numerical model for prediction of inhomogeneous failure properties of granitic rocks. Lemy and Hadjigeorgiou [9] developed a digital face mapping system for fast and safe acquisition of discontinuity network data using photographs of rock exposures. Geometrical parameters (length and orientation) of FIP were digitized using structural features [4].

To determine FILs from fluid inclusions, it is necessary to perform quantitative analysis of the geometrical and

*Corresponding author. Tel.: +86 21 5633 1972; fax: +86 21 5633 1971.
E-mail address: xjming@163.com (J. Xu).

1365-1609/$ - see front matter © 2007 Elsevier Ltd. All rights reserved.
doi:10.1016/j.ijrmms.2007.01.003

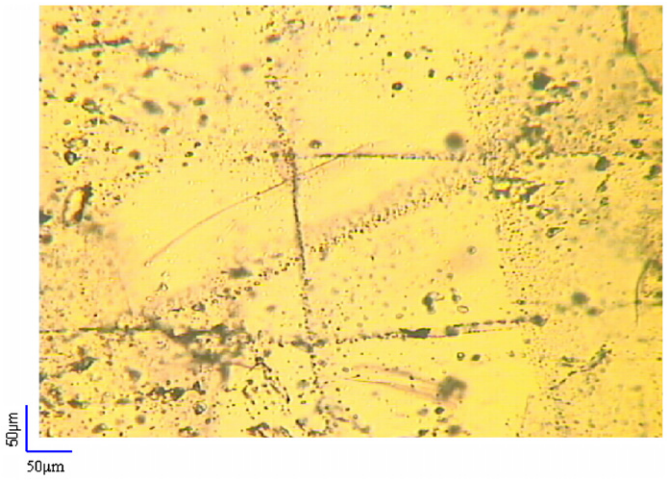

Fig. 1. An original image of fluid inclusions.

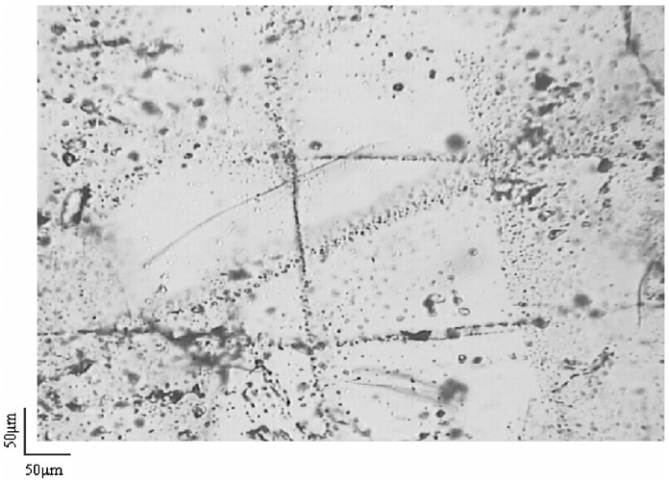

Fig. 2. Grayscale image converted from the original image.

configuration parameters of the fluid inclusions around the FIL [10]. The major parameters for individual fluid inclusions include [11,12]: (1) configuration parameters, such as area, shape, long- and short axis; and (2) geometrical parameters, such as centroid coordinates, intersection angle of long axis with coordinate axes. These parameters were considered in the analyses presented in this paper. Since the natural distributions of fluid inclusions are complicated and different FILs intersect each other, it is difficult to do the analyses using conventional methods.

The main purpose of this note is to determine the microcrack network in rocks using digital image analysis by evaluating the geometrical and configuration parameters of fluid inclusions. The determination procedures were coded into a program and could be run automatically. All of the original digital images were taken with the microscope equipped with a digital camera on a heating-freezing platform. The work allows for effective determination of FILs from fluid inclusions and investigation of the relationship between FIL network and crack properties in rocks. Because fluids trapped as inclusions in mode I cracks have been related to a specific deformational event [4], this approach is also potentially applicable to studying other geological phenomena, such as the forecast of the landslide happened in a rock slope [13].

Fig. 1 shows a typical digital image of fluid inclusions in rocks, which will be used to present the procedures of the proposed digital image analysis method. Other images of fluid inclusions were analyzed following the same procedures but are not presented herein considering the limits of space.

2. Analysis of the image of fluid inclusions

The original digital image was first converted into a grayscale image and then broken into blocks by quadtree decomposition and region segmentation. For each block, the inflection point (such as the Roberts, Prewitt and Sobel algorisms), derivative (such as the Canny algorisms [14] and Laplacian of Gaussian operator or LOG [15,16]), frequency and color-based methods were used to detect the

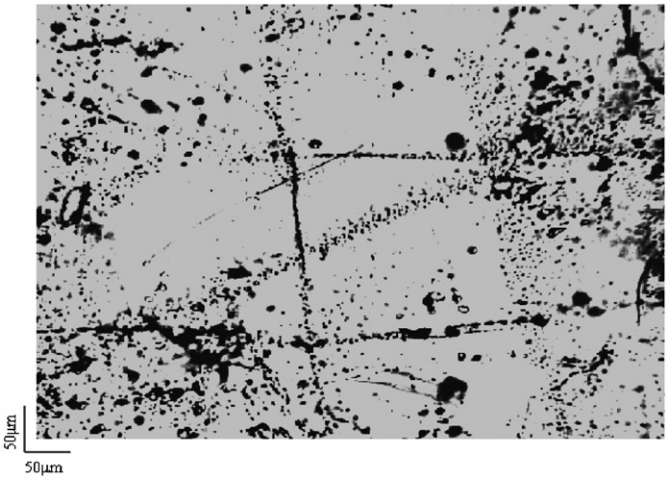

Fig. 3. Enhanced grayscale image.

edges of fluid inclusions. The methods used for the analysis of the image of fluid inclusions include image conversion, enhancement, segmentation, edge-detection and mathematical morphological treatment, which are summarized in the following.

2.1. Pre-processing of image

The original image from a microscope is a virtual image with the format of RGB (where R, G, B stand for red, green, blue, respectively) and the size of $M \times N \times 3$ pixels (where M and N are integers). For the ease of later processing and analysis, this image was converted into an image with grayscale values ranging from 0 to 255, size of $M \times N$ and grayscale function $f(x,y)$ [17]:

$$f(x,y) = \begin{bmatrix} a(1,1) & a(1,2) & \dots & a(1,N) \\ a(2,1) & a(2,2) & \dots & a(2,N) \\ \dots & \dots & \dots & \dots \\ a(M,1) & a(M,2) & \dots & a(M,N) \end{bmatrix}, \quad (1)$$

where x and y are the Cartesian coordinate positions in the image, a (x,y) is the grayscale value in the position (x,y), and $x = 1, 2,\ldots, M$; $y = 1, 2,\ldots,N$. The converted image is shown in Fig. 2. To further distinguish the inclusions from the backgrounds, the grayscale image was gray enhanced as shown in Fig. 3.

Since the whole image contained a huge amount of information, the enhanced image was segmented into blocks for analyses. The segmentation methods used include quadtree decomposition and region segmentation. In quadtree decomposition, the image was decomposed into the blocks with the size of $m \times m$ (where m was integer powers of 2). In region segmentation, the size of segmentation region was computed out from practical size of the image.

2.2. Recognition of fluid inclusions

Two methods were used for recognition of fluid inclusions: the ordinary edge-detection method and the color-based method.

Because of the obvious color differences between the fluid inclusions and the background, grayscales change smoothly along the tangent directions and intensely in the perpendicular directions of inclusion edges. These changes were described as the change of grayscale ratios and directions, or the magnitudes and directions of gradient vectors. For the direction derivative of function f (x,y), there were local maximum values or inflection points along inclusion edges, and the first and second derivatives reach the maximum and zero, respectively. The corresponding edge-detection operators can be classified into two types: the inflection point method (such as Robert, Prewitt and Sobel algorithms) and derivative method (such as the LOG [15,16] and Canny algorisms [14]). Because the grayscale frequency of fluid inclusions distributed in a relatively narrow range, a special algorism called the frequency method was used to detect edges of inclusions for each block. Edge-detection procedure was performed by dynamically selecting adaptable algorisms and adjusting related parameters. These parameters include thresholds, errors, detection directions (vertically, horizontally or both). The image after ordinary edge detection is shown in Fig. 4.

When the color-based method was used, the image was first converted from the RGB color space into the HIS color space (where H, I, S stand for hue, intensity and saturation, respectively) [18]. The inclusions were then extracted out by randomly selecting an inclusion in the image based on the specified thresholds. Fig. 5 shows the image after edge detection using the color-based method.

2.3. Mathematical morphological analysis of the image of fluid inclusions

Even though the outlines of fluid inclusions could be displayed approximately after edge detection, some outlines were discontinuous or un-smooth and these edges should be connected in a mathematical morphological sense. Mathematical morphological analysis is a technique for analyzing geometrical structure of the metallic or geologic samples, in which the basic operators are dilation and erosion and their combination. Dilation D (x,y), erosion E (x,y), opening O (x,y) and closing C (x,y) of a grayscale image F (x,y) and a structuring element B (x,y) are, respectively, defined by [17,19]

$$D(x,y) = (F \otimes B)(x,y) = \max\{F(x-s, y-t) + B(s,t)\}, \tag{2}$$

$$E(x,y) = (F \oplus B)(x,y) = \min\{F(x+s, y+t) - B(s,t)\}, \tag{3}$$

$$O(x,y) = ((F \oplus B) \otimes B)(x,y), \tag{4}$$

$$C(x,y) = ((F \otimes B) \oplus B)(x,y), \tag{5}$$

where s and t are dynamic integers in the above four transformations.

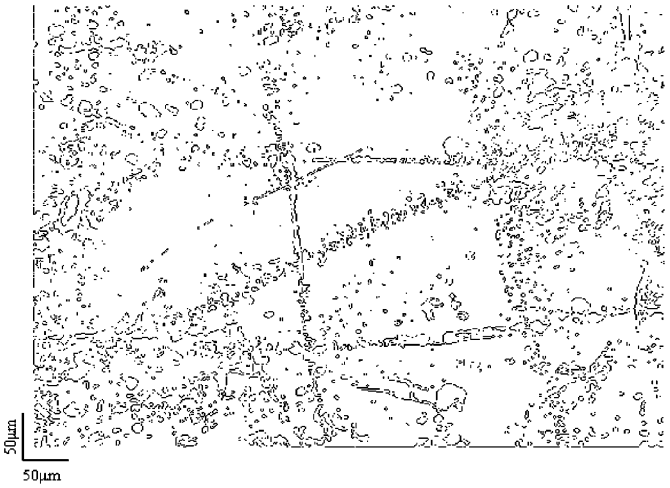

Fig. 4. The image after ordinary edge detection.

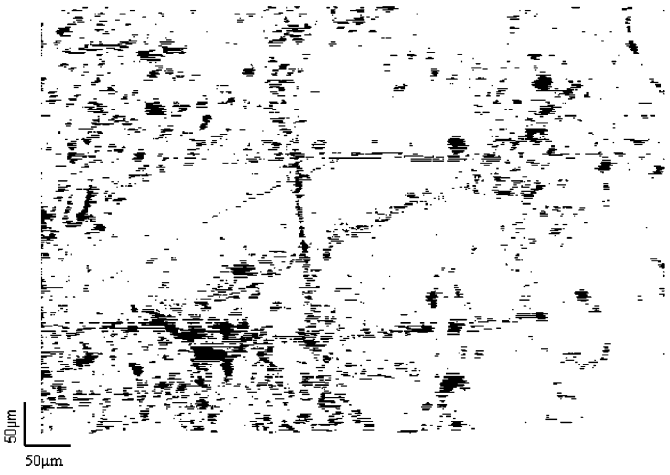

Fig. 5. The image after edge detection using color-based method.

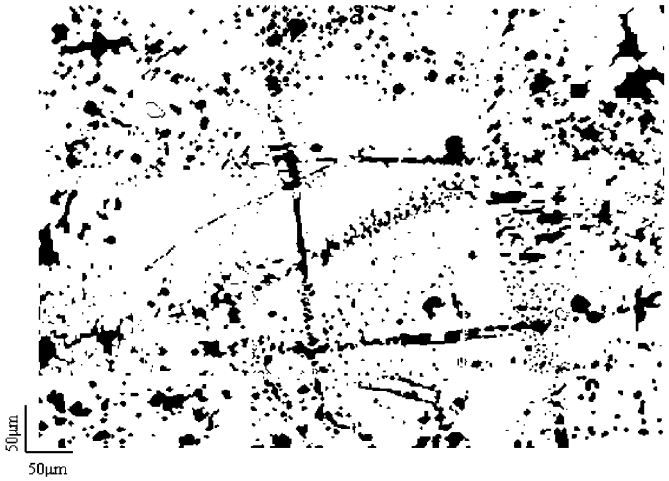

Fig. 6. The image after mathematical morphological analysis.

During the connecting process, the dilation, erosion and seed-filling techniques were used to connect discontinuous points and fill pores in the outlines. The boundary-linking technique was also used to separate fluid inclusions from boundaries and keep only the edges between the inclusions and the background. The protruding parts on the outlines were further treated using the smoothening technique. Fig. 6 shows the image after the mathematical morphological analysis.

During the mathematical morphological analysis, the related parameters (such as thresholds, algorism types and values of structural elements) could be assumed for the whole image or dynamically adjusted for each block in order to repeatedly use the data information.

3. Information extraction and combination

In order to consider the edge points or lines of individual inclusions in the global coordinate system, blocks were re-oriented and the data of the inclusions were separated and saved in the corresponding matrices. At the same time, the geometrical and configuration parameters extracted from the binary images [9] for each inclusion were saved in the computer. The parameters include the centroid positions g (x,y), areas A, long-axis R_l, short-axis R_s, perimeter P_c, intersection angles (θ_1, θ_2) of the long- and short axes with the horizontal coordinate axis.

For the ease of analysis, the small neighboring inclusions (say, n in total) were aggregated into large one following the steps below:

(1) computing centroid positions g_i (x,y) $i = 1,\ldots,n$ and distances L_i from g_i (x,y) to aggregated positions G (x,y) for each inclusion;
(2) computing the area A_1 of the aggregated inclusion;
(3) computing the centroid position G (x,y), equivalent area A_2, long-axis R_l. (the short-axis R_s, intersection angles (θ_1, θ_2) of long- and short axes with the horizontal coordinate axis may be determined in the same way).

Table 1
Configuration parameters for FIL

Numbers of FIL	Total number of inclusions	MXD (μm)	MND (μm)	MD (μm)
FIL01	160	35.9	0.071	11.8
FIL02	90	26.8	0.018	8.9
FIL03	99	40	0.214	10.1
FIL04	88	38.1	0.464	11.7
FIL05	193	57.1	0.511	18.3
FIL06	25	13.7	0.444	5.1

L, A_1, A_2 and R_1 were, respectively, expressed as

$$L<\gamma R_1', \quad A_1 = \lambda \sum_{i=1}^{n} A_i/n, \tag{6}$$

$$A_2 = \sum_{i=1}^{n} A_i, \quad R_1 = \sum_{i=1}^{n} A_i R_{li} / \sum_{i=1}^{n} A_i, \tag{7}$$

where R_1' was the maximum of long axes; and λ and γ were coefficients.

If there were small inclusions around an existing large one, the small and large inclusions were aggregated into new larger one. In aggregation, the centroid position and the angles between the long-, short-axes and the horizontal axis of the large inclusion remained unchanged but the areas of all small inclusions were added into that of the large one. After aggregation, this new larger inclusion was taken as an individual to calculate the related geometrical or configuration parameters.

After the above operations, the configuration parameters were obtained for fluid inclusion lines, or FIL. These parameters were shown in Table 1, in which MXD, MND, and MD are, respectively, the maximum, minimum and mean distances between the centroids of inclusions and FIL.

4. Curve fitting of FILs

Because many fluid inclusions existed near a virtual FIL, the positions and related mathematical expressions of FILs were determined from the centroid coordinates of all inclusions. Given n inclusions, the centroid position g_i (x,y) $(i = 1,\ldots,n)$ of each inclusion was first used to simulate a curve S_1 with the least-squares method [20] and the distance d_i between g_i (x,y) and S_1 was obtained. The area A_i, the long-axis direction θ_{1i} and the distance d_i of the ith inclusion were then used as dependant variables to construct a weight function $\{\omega_i\}$:

$$\omega_i = \frac{A_i\theta_{1i}/d_i}{\sum_{i=1}^{n} A_i\theta_{1i}/d_i}. \tag{8}$$

At last, the centroid positions g_i (x,y) were used as a point set, ω_i as a weight function and the least-squares

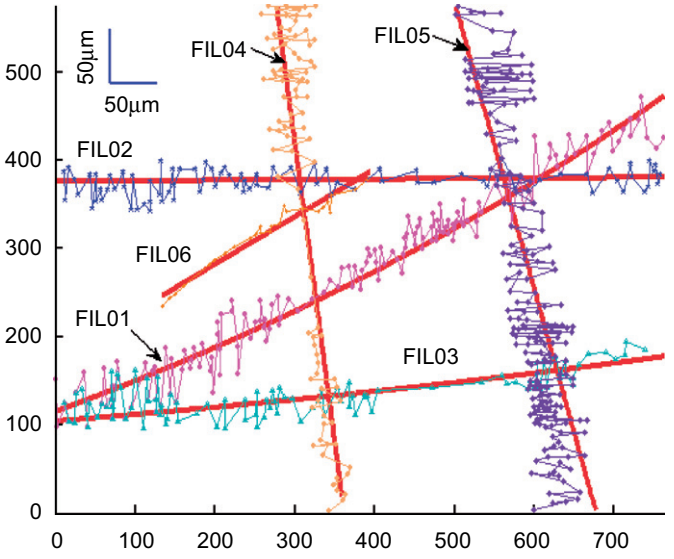

Fig. 7. Images of FILs.

method was again used to fit curve S^*:

$$S^*(x) = \sum_{k=1}^{n} \alpha_k^* P_k(x), \tag{9}$$

where a_k^* was the coefficient calculated from

$$a_k^* = \frac{\sum_{i=1}^{n} \omega_i f_i P_k(x_i)}{\sum_{i=1}^{n} \omega_i p_k^2(x_i)}, \tag{10}$$

where $P_k(x)$ is the normal polynomial with weights $\{\omega_i\}$; k the integers, where $k = 1, 2, \ldots, m-1$; and m is the item number of $P_k(x)$. The fitted FILs are shown in Fig. 7.

5. Characteristics of FIL

According to the fitted FILs, the length, mean width and abundance for each FIL were finally obtained and shown in Table 2. In Table 2, S is the arc length of a FIL, B is the mean of outer widths of fluid inclusions near FILs, and ρ is the abundance of fluid inclusions along a FIL:

$$\rho = \frac{\sum_{i=1}^{n} A_i / R_{\mathrm{si}}}{S} \times 100\%, \tag{11}$$

where R_{si} is the length of short axis for the ith inclusion and A_i the area of the ith inclusion.

The relationships between the locations of FILs were classified into two types: parallel and intersecting. The former were called type A and the latter type B. Fig. 8 shows the distances or intersection angles between these two types of FILs.

Table 3 shows the intersection angles and distances between FILs. The data above and below the diagonal line are, respectively, the intersection angles in degrees and distances in μm between FILs.

Table 2
Characteristic parameters of FILs

Characteristic parameters	Lengths, S (μm)	Mean widths, B (μm)	Abundances, ρ (%)
FIL01	655.2	174.83	11.591
FIL02	592.11	174.36	6.9404
FIL03	594.88	178.71	17.135
FIL04	580.47	161.72	18.197
FIL05	460.95	158.48	9.9579
FIL06	229.77	59.914	0.3503

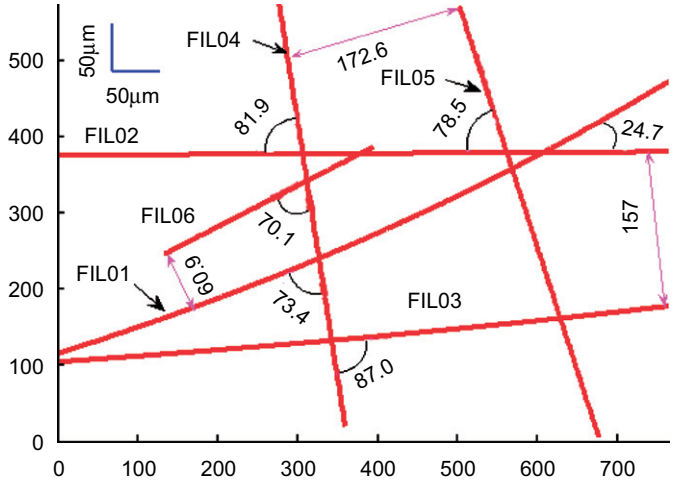

Fig. 8. Two types of FILs: parallel and intersecting.

Table 3
Intersection angles and distances between FILs

	FIL01	FIL02	FIL03	FIL04	FIL05	FIL06
FIL01		24.7	19.7	73.4	82.1	0
FIL02	0		0	81.9	73.2	28.0
FIL03	0	157.0		87.0	78.4	0
FIL04	0	0	0		0	70.1
FIL05	0	0	0	172.6		0
FIL06	60.9	0	101.7	0	122.4	

According to Table 3, Fig. 8 and the regional geological conditions [21]

(1) type A FILs (such as FIL01 and FIL06, FIL02 and FIL03, FIL04 and 05) are almost parallel to each other. The corresponding cracks were formed mainly from tension activities and have relatively great width, irregular surface, short penetrative length and small roughness;
(2) type B FILs (such as FIL01 and FIL03, FIL02 and FIL04, FIL03 and 06) intersect with each other. The fluid inclusions around the type B FILs have relatively regular shapes, small areas and densely distributions. The bisector directions of FILs are in agreement with the directions of major principal stresses for crack

formation and the cracks were formed mainly from rock sliding or shearing-compression activities.

6. Conclusions

Digital image analyses of fluid inclusions in rocks were successfully performed. For the ease of analysis, the image taken by a microscope on a heating–freezing platform were converted into grayscale images and broken into blocks by image segmentations. For each block, the inflection point, derivative, frequency and color-based methods were used to detect edges of fluid inclusions. The dilation, erosion, seed filling, boundary connection and smoothening methods were all used to solve the problems related to discontinuous points and projecting parts for the edges of fluid inclusions. According to the properties of inclusions, fluid inclusion lines and their configuration parameters were then obtained using least-squares method. The analysis procedures were carried out by author's special program.

The relationships between the network of fluid inclusion planes and the properties of cracks in rocks were initially studied. The fluid inclusion lines could relatively well reflect crack characteristics such as trending, length, intersection angle, etc. The types or distributions of FILs were in good agreement with the corresponding cracks. Therefore, the digital image analysis of fluid inclusions in rocks may be used to study the cracks in rocks.

Acknowledgments

Financial support for the study was provided by the Natural Sciences Foundation Committee of China under Grant no. 40572162. This support is gratefully acknowledged. The authors are grateful to Mark Lespinasse and an anonymous reviewer for their valuable suggestions, and to Lianyang Zhang and Jie Han for improving the English of the paper and other suggestions.

References

[1] Lespinasse M. Are fluid inclusion planes useful in structural geology? J Struct Geol 1999;21:1237–43.
[2] Hoxha D, Lespinasse M, Sausse J, Homand F. A microstructural study of natural and experimentally induced cracks in a granodiorite. Tectonophysics 2005;395:99–112.
[3] Goldstein RH. Fluid inclusions in sedimentary and diagenetic systems. Lithos 2001;55:159–93.
[4] Lespinasse M, Désindes L, Fratczak P, Petrov P. Microfissural mapping of natural cracks in rocks: implications on fluid transfers quantification in the crust. Chem Geol 2005;223:170–8.
[5] Lespinasse M, Cathelineau M. Paleostress magnitudes determination by using fault slip and fluid inclusions planes (FIP) data. J Geophys Res 1995;100:3895–904.
[6] Zhao XB, Xu JM. Digital properties of geo-material images. In: Luan MT, Zen K, Chen GQ, Nian TK, Kasama K, editors. Recent development and geo-environmental engineering in Asia, proceeding of the fourth Asian joint symposium on geotechnical and geo-environmental engineering. Dalian: Dalian University Technical Press; 2006. p. 71–4.
[7] Zhu WC, Liu J, Yang TH, Sheng JC, Elsworth D. Effects of local rock heterogeneities on the hydromechanics of fractured rocks using a digital-image-based technique. Int J Rock Mech Min Sci 2006; 43:1182–99.
[8] Chen S, Yue ZQ, Tham LG. Digital image-based numerical modeling method for prediction of inhomogeneous rock failure. Int J Rock Mech Min Sci 2004;41:939–57.
[9] Lemy M, Hadjigeorgiou J. Discontinuity trace map construction using photographs of rock exposures. Int J Rock Mech Min Sci 2003;40:903–17.
[10] Li CY, et al. Theory and practice of computer graphics. Beijing: Beijing Aviation & Spaceflight University Press; 2003 (in Chinese).
[11] Tu XB, Wang SJ. Particle shape descriptor in digital image analysis. J Geotech Eng 2003;26:659–62 [in Chinese].
[12] Hu RL, Yue ZQ, Tham LG, Wang LC. Digital image analysis of dynamic compaction effects on clay fills. J Geotech Geoenviron Eng ASCE 2005;131:1411–22.
[13] Xu JM, Sun KL. Forecast of landslide boundary using the fluid inclusion method. China Civ Eng J 2007;40:69–73 [in Chinese].
[14] Canny J. A computational approach to edge detection. IEEE Trans Pattern Anal Mach Intell (PAMI) 1986;8:679–98.
[15] Huertas A, Medioni G. Detection of intensity changes with sub pixel accuracy using Laplacian–Gaussian masks. IEEE Trans Pattern Anal Mach Intell (PAMI) 1986;8:651–64.
[16] Zhao YQ, Gui WH, Chen ZC, Tang JT, Li LY. Medical images edge detection based on mathematical morphology. In: Proceedings of the IEEE 27th annual conference on engineering in medicine and biology, 2005. p. 6492–95.
[17] Gonzalez RC, Woods RE. Digtal image processing. 2nd ed. Beijing: Publishing House of Electronics Industry; 2005.
[18] Guerfi S, Gambotto JP, Lelandais S. Implementation of the watershed method in the HSI color space for the face extraction. Adv Video Signal Based Surveill 2005:282–6.
[19] Lee JSJ, Haralick RM, Shapiro LG. Morphologic edge detection. IEEE J Robotics Automat 1987;3:142–56.
[20] Shen JH. Foundations of numerical algorithm. Shanghai: Tongji University Press; 2004 [in Chinese].
[21] Liu B. Thermodynamics for hydrocarbon inclusions. Beijing: Science Press; 2005 [in Chinese].